# Star formation in massive protoclusters in the Monoceros OB1 dark cloud

G. Wolf-Chase,[1,2]⋆ G. Moriarty-Schieven,[3] M. Fich[4] and M. Barsony[5,6]

[1]*Department of Astronomy and Astrophysics, University of Chicago, 5640 S. Ellis Ave., Chicago, IL 60637, USA*
[2]*Adler Planetarium and Astronomy Museum, 1300 S. Lake Shore Drive, Chicago, IL 60605, USA*
[3]*National Research Council of Canada, 660 N. A'ohoku Place, Hilo, HI 96720, USA*
[4]*University of Waterloo, Department of Physics, Waterloo, Ontario, N2L 3G1, Canada*
[5]*Space Science Institute, 3100 Marine Street, Suite A353, Boulder, CO 80303-1058, USA*
[6]*Department of Physics and Astronomy, San Francisco State University, 1600 Holloway Avenue, San Francisco, CA 94132-4163, USA*

## ABSTRACT

We present far-infrared, submillimetre and millimetre observations of bright *IRAS* sources and outflows that are associated with massive CS clumps in the Monoceros OB1 dark cloud. Individual star-forming cores are identified within each clump. We show that combining submillimetre maps, obtained with SCUBA on the James Clerk Maxwell Telescope, with HIRES-processed and modelled *IRAS* data is a powerful technique that can be used to place better limits on individual source contributions to the far-infrared flux in clustered regions. Three previously categorized 'Class I objects' are shown to consist of multiple sources in different evolutionary stages. In each case, the *IRAS* point source dominates the flux at 12 and 25 μm. In two cases, the *IRAS* point source is not evident at submillimetre wavelengths. The submillimetre sources contribute significantly to the 60- and 100-μm fluxes, dominating the flux in the 100-μm waveband. Using fluxes derived from our technique, we present the spectral energy distribution and physical parameters for an intermediate-mass Class 0 object in one of the regions. Our new CO $J = 2 \to 1$ outflow maps of the three regions studied indicate complex morphology suggestive of multiple driving sources. We discuss the possible implications of our results for published correlations between outflow momentum deposition rates and 'source' luminosities, and for using these derived properties to estimate the ratio of mass ejection rates to mass accretion rates on to protostars.

**Key words:** techniques: image processing – stars: formation – ISM: individual: Mon OB1 – ISM: jets and outflows – radio lines: ISM.

## 1 INTRODUCTION

One of the outstanding questions in star formation is whether high-mass stars form in a similar manner to low-mass stars; but the answer to this question is poorly constrained observationally. Although the tendency for stars to form in clusters in regions of intermediate- and high-mass star formation has been firmly established (Testi, Palla & Natta 1999), the main data base for infrared data on these stellar nurseries remains that of *IRAS*, which typically probes large cloud structures identified with the formation of clusters or groups of stars (clumps), rather than the smaller condensations (∼0.1 pc – cores) out of which single stars or multiple stellar systems form (McKee 1999; Myers 1999).

For many years now, the *IRAS* data base has been used extensively to help categorize the spectral energy distributions (SEDs) of young stellar objects (YSOs) according to the proposed evolutionary scheme developed by Adams, Lada & Shu (1987). Although this scheme was originally proposed to describe an evolutionary sequence for isolated low-mass star formation, it has since been applied to many *IRAS* sources that are often high-luminosity objects, begging the question of what an SED means in cases where it describes not a single star-forming core, but rather a group of objects, which may or may not be coeval. Furthermore, since the earliest surveys for bipolar outflows in molecular clouds (Bally & Lada 1983; Lada 1985), the *IRAS* data base has been used extensively to help determine the luminosities of the driving sources of these outflows and to further establish correlations between source and outflow properties (e.g. Panagia 1991; Cabrit & Bertout 1992). A recent survey for jets in the Vela molecular clouds produced evidence that many jets are driven by low-mass objects clustered around *IRAS* sources that are likely to be intermediate-mass YSOs (Lorenzetti et al. 2002). This raises the interesting question of how the observed correlations between outflow momentum deposition rates and 'source' luminosities should be interpreted.

Submillimetre continuum imaging with arrays such as SCUBA (Submillimetre Common-User Bolometer Array) on the 15-m James

⋆Email: grace@horta.uchicago.edu

Clerk Maxwell Telescope (JCMT) on Mauna Kea can probe conditions on the scale of individual star-forming cores, and thus can be useful in separating sources in confused regions, but, by themselves, these observations yield limited spectral coverage for the determination of physical properties such as temperature, bolometric luminosity and evolutionary stage. Since protostars have SEDs that peak in the far-infrared, multiband infrared data are critical, though difficult to obtain given the current lack of operational far-infrared observatories. However, software advances in HIRES (high-resolution) processing of *IRAS* data (Aumann, Fowler & Melnyk 1990) have allowed unprecedented spatial resolutions to be achieved at far-infrared wavelengths (Surace et al. 1993; Terebey & Mazzarella 1994; Cao et al. 1996; Hurt & Barsony 1996; Cao et al. 1997; Barsony et al. 1998). HIRES processing and modelling of *IRAS* data has even been suggested as a method for identifying Class 0 protostars (O'Linger et al. 1999).

In this paper, we apply HIRES processing and modelling techniques to massive star-forming clumps in the Monoceros (Mon) OB1 dark cloud. Molecular emission from the Mon OB1 dark cloud was first mapped by Blitz (1978) at low resolution covering 11 deg$^2$ towards the arc of dark nebulae seen on the Palomar Observatory Sky Survey print (Lynds 1962). Since the Mon OB1 dark cloud lies towards the outer Galaxy, near the Galactic anticentre, confusion due to foreground and background clouds is at a minimum, affording an excellent opportunity to study the large-scale distribution of molecular material and associated star formation. Oliver, Masheder & Thaddeus (1996, hereafter OMT96) performed an unbiased CO survey over 52 deg$^2$ at higher sensitivity and spectral resolution than the Blitz survey in order to gain a better understanding of the large-scale structure and kinematics of the interstellar medium (ISM) towards the Mon OB1 region and to study the properties of molecular clouds in the outer Galaxy. They used the *IRAS* Point Source Catalogue to identify sites of massive star formation in their large-scale CO survey by applying two criteria using colour selection of *IRAS* point sources (Richards et al. 1987; Wood & Churchwell 1989).

The star-forming region that OMT96 identify as Cloud 16, associated with the young star cluster NGC 2264, has been the target of many molecular line studies, including an unbiased CO $J = 1 \rightarrow 0$ survey for molecular outflows (Margulis, Lada & Snell 1988, hereafter MLS88) and search for dense gas via a multitransitional CS study (Wolf-Chase, Walker & Lada 1995, hereafter WWL95; Wolf-Chase & Walker 1995, hereafter WW95). Prior to publication of the *IRAS* Point Source Catalogue, Margulis, Lada & Young (1989, hereafter MLY89) used the *IRAS* data base to identify 30 discrete sources within this region, and classify their SEDs in terms of the evolutionary scheme proposed by Adams et al. (1987). Four of these sources lie at or near the emission peaks of the CS clumps identified by WWL95: IRAS 9 (IRAS 06382+0932; also NGC 2264 IRS 1– Allen 1972), IRAS 12 (IRAS 06382+0939), IRAS 25 (IRAS 06382+1017) and IRAS 27 (IRAS 06381+1039). Three of these sources are also identified as sites of massive star formation by OMT96 (IRAS 06382+0939, 06382+1017 and 06381+1039). All three of these *IRAS* sources were categorized as Class I objects by MLY89.

The primary goal of this paper is to identify individual star-forming cores located in the massive CS clumps in Mon OB1 and estimate their contributions to the *IRAS* fluxes that characterize the entire clumps, in order to assess the accuracy of source classes and luminosities that were previously deduced from the *IRAS* data. We concentrate on the three sites of massive star formation identified by OMT96, since the fourth *IRAS* source that coincides with a CS

emission peak, NGC 2264 IRS 1, has already been studied in great detail in both molecular line and continuum emission (e.g. Schreyer et al. 1997; Ward-Thompson et al. 2000; Wang et al. 2002). In addition to the *IRAS* Point Source Catalogue designations, we use the nomenclature of MLS88 and MLY89 to refer to outflows and *IRAS* sources in this cloud. We adopt a distance to Mon OB1 of 800 pc (Walker 1956), the same distance adopted by MLS88 and MLY89. This is a compromise between more recent estimates of $700 \pm 40$ pc and 790 pc given by Feldbrugge & van Genderen (1991) and Sagar & Joshi (1983) based on *VBLUW* and *UBV* photometry of stars in the young cluster NGC 2264, and 950 pc, adopted by OMT96, based on photometric analysis by Pérez, Thé & Westerlund (1987).

## 2 OBSERVATIONS AND DATA REDUCTION

### 2.1 Submillimetre continuum mapping: JCMT observations

The observations presented here were obtained with SCUBA (Holland et al. 1999) at the JCMT[1] located near the summit of Mauna Kea, Hawaii. The instrument contains two arrays of bolometric detectors – the Short Wave (SW) array has 91 pixels optimized for observations at 450 μm, and the Long Wave (LW) array has 37 pixels at 850 μm. Both arrays can be used simultaneously and have approximately a 2.3-arcmin diameter field of view on the sky. The instrument achieves sky-background-limited performance by cooling the detectors to ∼75 mK.

The data were obtained 1999 August 9, November 18 and 23, and 2000 October 21, using the standard SCUBA 'scan-map' observing mode (Jenness et al. 2000). Fully sampled maps at both 450 and 850 μm were generated with 3-arcsec sampling. The pointing was checked using a nearby blazar every ∼1 h, and was found to vary by <2 arcsec. The data were corrected for atmospheric extinction by the method recommended by Archibald et al. (2002), i.e. fitting a polynomial to the 225-GHz zenith optical depth derived by a tipping radiometer, then extrapolating to 850 and 450 μm. The data were reduced and maps reconstructed using the ORAC data reduction package (Jenness & Economou 2001).

Flux calibration was applied to the data using images of a planet or of the secondary calibrator source CRL618, obtained using the same observing technique as the data. Flux densities of the sources were derived using aperture photometry with a 45-arcsec diameter aperture, and then correcting for flux in the error beam using the same flux calibration images.

### 2.2 NRAO 12-m continuum photometry

We obtained 1.3-mm continuum data during 1997 December, using the National Radio Astronomy Observatory (NRAO) 12-m telescope located on Kitt Peak, near Tucson, Arizona,[2] towards the position of three compact submillimetre sources that we identified in earlier, unpublished, 850-μm SCUBA jiggle maps, which we

---

[1] The JCMT is operated by the Joint Astronomy Centre on behalf of the Particle Physics and Astronomy Research Council of the United Kingdom, the Netherlands Organization for Scientific Research, and the National Research Council of Canada.

[2] The National Radio Astronomy Observatory is a facility of the National Science Foundation, operated under cooperative agreement by Associated Universities, Inc. The 12-m telescope (currently known as the Arizona Radio Observatory) is now operated through the University of Arizona's Steward Observatory, with funds provided by the University of Arizona, the Research Corporation, and the National Science Foundation.

acquired prior to the scan maps reported in this paper. We measured the 1.3-mm continuum flux towards these sources within a 27-arcsec beam using a dual-channel, double-sideband, SIS heterodyne receiver system. The receiver had a bandwidth of 600 MHz and was operated at a sky frequency of 231.6 GHz. The subreflector was nutated at a frequency of 4 Hz, using a 2-arcmin beam throw. Data were calibrated by chopping between sky and an ambient temperature load. Owing to the inopportune positions of the planets, absolute calibration was achieved by observing NGC 2071 IR and NGC 2264 IRS, and using published 1.3-mm fluxes to scale our data (Walker, Adams & Lada 1990; Sandell 1994). Consequently, we estimate 1.3-mm flux uncertainty to be at the 30–40 per cent level.

### 2.3 Far-infrared mapping: HIRES processing of the *IRAS* data

A detailed background of *IRAS* data and HIRES processing techniques may be found in Hurt & Barsony (1996), Barsony et al. (1998) and O'Linger et al. (1999), including an in-depth discussion of the significant merits of taking HIRES processing beyond the standard 20 iterations, which is the default when HIRES processing is requested remotely via electronic mail to IPAC.[3] For the data presented here, we halted HIRES processing at 40 iterations in the 12 and 25-$\mu$m bands, and at 200 iterations in the 60 and 100-$\mu$m bands. These images do not represent 'converged' data in a formal sense, as the concept of convergence in iterative solutions of nonlinear problems seldom has any absolute meaning (O'Linger et al. 1999). Our iteration limits in the various wavebands were chosen by looking at the change in the correction factor variance from one iteration to the next, and setting an acceptable threshold value (Aumann et al. 1990; Hurt & Barsony 1996; O'Linger 1997; Barsony et al. 1998).

The irregular sampling of the sky brightness distribution by subsequent passes of the *IRAS* detectors results in variable spatial resolution across a HIRES-processed image. Among the diagnostic maps produced during the HIRES processing are 'beam-sampled' maps, which may be used to compute effective resolutions achieved at various positions in the HIRES-processed image by inputting a series of user-defined, point-source 'spikes' across the image. These spikes are then HIRES-processed along with the actual *IRAS* data, allowing effective resolutions to be calculated at the positions of the spikes. Ideally, the beam-sampled maps can be used to produce models of the actual HIRES-processed *IRAS* emission. For example, supplying user-defined spikes to coincide in magnitude and position with actual sources chosen from the *IRAS* Point Source Catalogue results in a point-source model that can be compared to the actual HIRES-processed data (Hurt & Barsony 1996). One may subsequently add further spikes to more closely simulate the actual emission (O'Linger 1997; Barsony et al. 1998). Such spikes may represent extended emission, or, in some cases, additional embedded sources. Point-source modelling offers significant advantages over simple software aperture photometry of the HIRES-processed *IRAS* survey images. Whereas simple software aperture photometry suffers from uncertainties as to the proper aperture size to use, and the systematic effects that can be introduced by the processing algorithm itself, the input fluxes for the best-matching image to the *IRAS* survey data in point-source models are known.

In some cases, higher-resolution observations may be available at a different wavelength, which can be used to estimate placement of input spikes. Our high-resolution (14 arcsec at 850 $\mu$m; 7 arcsec at 450 $\mu$m) SCUBA observations have given us prior knowledge of sources that are embedded in dense cores in the Mon OB1 dark cloud. We have used this prior knowledge to model the HIRES-processed *IRAS* emission from these sources. The default pixel size of 15 arcsec was used. Absolute calibration uncertainty for HIRES-derived fluxes is estimated to be 20 per cent (Levine & Surace 1993).

### 2.4 NRAO 12-m OTF mapping

We acquired CO $J = 2 \rightarrow 1$ maps of outflows NGC 2264 O and 2264 H (associated with MLY89 sources IRAS 25 and 27) using the spectral-line on-the-fly (OTF) mapping mode of the NRAO's 12-m telescope in 1996 March, and of NGC 2264 D (associated with MLY89 source IRAS 12) in 1999 May. The OTF technique allows the acquisition of large-area, high-sensitivity, spectral line maps with unprecedented speed and pointing accuracy.

A dual-channel, single-sideband SIS receiver was used for all observations. For the 1996 March observations, the back-end consisted of a 1536-channel hybrid spectrometer. The 1536 channels were divided among the two receiver polarization channels. A bandwidth of 600 MHz, yielding a spectral resolution of 781 kHz (1 km s$^{-1}$), was used for NGC 2264 O, and a bandwidth of 300 MHz, yielding a spectral resolution of 391 kHz (0.5 km s$^{-1}$), was used for NGC 2264 H. For the 1999 May observations of NGC 2264 D, the back-end consisted of 500 kHz and 1 MHz resolution filter-banks, yielding velocity resolutions of 0.65 and 1.3 km s$^{-1}$, respectively. The filter-banks were used in parallel mode, each of the two receiver polarization channels using 256 filter-bank channels. The polarization channels were subsequently averaged together to improve signal-to-noise ratio. Only the 500-kHz resolution data were used to produce the final map. We performed five map coverages for each outflow, attaining an rms $\sim$ 0.25–0.35 K for the added maps. We used the NRAO standard source Orion A ($\alpha_{1950} = 05^{\mathrm{h}}32^{\mathrm{m}}47\overset{\mathrm{s}}{.}0$, $\delta_{1950} = -05°24'21''$) to check absolute line temperatures.

The OTF data were reduced with the Astronomical Image Processing Software (AIPS), version 15JUL95. AIPS tasks specific to OTF data are OTFUV, which converts a single 12-m OTF map (in UniPOPS SDD format) to UV (single-dish) format, and SDGRD, which selects random-position single-dish data in AIPS UV format in a specified field of view about a specified position and projects the coordinates on to the specified coordinate system. The data are then convolved on to a grid. OTF data maps were first combined, then gridded into a data cube and baseline-subtracted. Channel maps as well as individual spectra were inspected to ensure good baseline removal and to check for scanning artefacts.

## 3  RESULTS

### 3.1  Background

#### 3.1.1  IRAS 06382+0939 (IRAS 12)

IRAS 12 was classified as a Class I object by MLY89. Identified as IRAS 06382+0939 upon publication of the Point Source Catalogue, it is embedded in the northern part of a massive (1900–2500 M$_\odot$) clump traced by CS $J = 2 \rightarrow 1$ emission (WWL95). *J*, *H*, *K* and *L'* maps of the *IRAS* source revealed two point sources (RNO-East and RNO-West) separated by 2.8 arcsec along a position angle of

---

[3] IPAC is funded by NASA as part of the *IRAS* extended mission under contract to JPL.

265° at the PSC position (Castelaz & Grasdalen 1988). The effective temperatures of RNO-East and RNO-West were found to be 3000 and 10 000 K, respectively, with a combined luminosity of about 550 L$_{\odot}$. The age of RNO-East was found to be less than $10^5$ yr old, and RNO-West was found to be a young high-mass star (Castelaz & Grasdalen 1988). This region was also previously observed in the far-infrared at 70 and 130 μm (Sargent et al. 1984) and from 40 to 160 μm (Cohen, Harvey & Schwartz 1985). The latter reported a double peak, based on the higher-resolution (40–45 arcsec) capabilities of the Kuiper Airborne Observatory (KAO): their primary peak corresponds to the position of the *IRAS* PSC position, while their secondary peak lies more than 2 arcmin to the south-east, approximately at the peak of the CS $J = 2 \rightarrow 1$ and CS $J = 5 \rightarrow 4$ emission reported by WWL95.

MLS88 associated IRAS 12 with a large (≈12 arcmin in extent), massive (16–30 M$_{\odot}$), bipolar, CO outflow (NGC 2264 D), oriented with its major axis along a north-east–south-west (NE–SW) direction, which has a dynamic time-scale of ∼$6.9 \times 10^4$ yr. High-velocity wings associated with the outflow were also observed in CS $J = 2 \rightarrow 1$ spectra (WW95). The outflow centroid is displaced ∼2 arcmin from the *IRAS* PSC position. A weak (≈0.6 mJy) VLA 6-cm source, a strong H$_2$O maser and four near-infrared sources all lie within the boundaries of the outflow, distributed in a band approximately perpendicular to the outflow axis. One of the near-infrared sources (IRS A) was identified as the probable driving source of the outflow, based on its location closest to the outflow centroid of all the near-infrared sources (Mendoza et al. 1990).

### 3.1.2  IRAS 06382+1017 (IRAS 25)

IRAS 25 was classified as a Class I object by MLY89. Identified as IRAS 06382+1017 upon publication of the Point Source Catalogue, it lies at the southern end of an extended, massive (500–700 M$_{\odot}$) clump traced by CS $J = 2 \rightarrow 1$ emission (WWL95). It has been associated with a compact CO outflow, NGC 2264 O (WWL95; WW95); a giant Herbig–Haro flow, HH124, and its bow-shock pairs, HH124-E and HH124-W; an infrared reflection nebula; and a near-infrared source (Walsh, Ogura & Reipurth 1992;

Moneti & Reipurth 1995; Ogura 1995; Piché, Howard & Pipher 1995). The near-infrared source is a barely resolved binary, with the secondary component located ∼1.75 arcsec (∼1400 au) from the primary at a PA ≈ 155°. The Herbig–Haro objects lie along a PA ≈ 105°, while the infrared reflection nebula lies along a PA ≈ 45°. Piché et al. (1995) suggested that the infrared reflection nebulosity might be due to the lobes of a second outflow cavity extending towards the north-east, or, alternatively, reflection off a circumstellar torus whose polar axis is roughly parallel to the axis of the Herbig–Haro flow. Rodríguez & Reipurth (1998) reported two VLA sources within the error ellipse for *IRAS* 06382+1017 [VLA1: $\alpha(1950) = 06^h38^m17\overset{s}{.}01$, $\delta(1950) = +10°17'56\overset{''}{.}2$; VLA2: $\alpha(1950) = 06^h38^m17\overset{s}{.}91$, $\delta(1950) = +10°17'58\overset{''}{.}3$]. VLA 1 is approximately coincident with the position of the near-infrared source and reflection nebula.

### 3.1.3  IRAS 06381+1039 (IRAS 27)

IRAS 27 was classified as a Class I object by MLY89. Identified as IRAS 06381+1039 upon publication of the Point Source Catalogue, it lies near the northern end of a massive (500–700 M$_{\odot}$) clump traced by CS $J = 2 \rightarrow 1$ emission (WWL95). MLS88 associated this source with an outflow that they identified as having a shorter axis along the direction of the outflow than perpendicular to the direction of the outflow (NGC 2264 H). The *IRAS* source is offset about 45 arcsec west of the apparent outflow centre. A striking asymmetry is seen in the velocity extents of the blue- and redshifted gas; the redshifted gas is evident from 10–30 km s$^{-1}$, while the blueshifted gas was seen only from 0–3 km s$^{-1}$. The mass of this outflow was computed to be $M_{\text{flow}} = 1.6$–2.3 M$_{\odot}$; and its dynamic time-scale, $\tau_d = 1.2 \times 10^4$ yr, makes it the second youngest of the nine outflows mapped by MLS88. High-velocity wings associated with the outflow were also observed in CS $J = 2 \rightarrow 1$ spectra (WW95).

### 3.2  SCUBA images

In this section, we present our 450- and 850-μm SCUBA maps of the *IRAS* sources. Table 1 lists 450- and 850-μm fluxes for all the

**Table 1.** Mon OB1 SCUBA and millimetre source fluxes.

| Source | $\alpha$(2000) | $\delta$(2000) | Flux (Jy) | | |
|---|---|---|---|---|---|
| | | | 450 μm | 850 μm | 1300 μm |
| RNO | $06^h41^m02\overset{s}{.}8$ | $09°36'10''$ | <29.6 | <1.86 | ... |
| 12 S1 | $06^h41^m05\overset{s}{.}8$ | $09°34'09''$ | $47.9 \pm 0.51$ | $5.38 \pm 0.019$ | $1.4 \pm 0.49$ |
| 12 S2 | $06^h41^m06\overset{s}{.}2$ | $09°35'57''$ | $57.0 \pm 0.51$ | $5.35 \pm 0.019$ | ... |
| 12 S3 | $06^h41^m04\overset{s}{.}1$ | $09°35'01''$ | $47.9 \pm 0.51$ | $4.94 \pm 0.019$ | ... |
| 12 S4 | $06^h41^m00\overset{s}{.}9$ | $09°35'28''$ | $42.1 \pm 0.51$ | $4.15 \pm 0.019$ | ... |
| 12 S5 | $06^h40^m49\overset{s}{.}3$ | $09°34'36''$ | $16.20 \pm 0.51$ | $2.171 \pm 0.019$ | ... |
| 12 S6 | $06^h40^m57\overset{s}{.}8$ | $09°36'25''$ | $32.34 \pm 0.51$ | $2.986 \pm 0.019$ | ... |
| 12 S7 | $06^h41^m11\overset{s}{.}6$ | $09°35'34''$ | $26.40 \pm 0.51$ | $2.652 \pm 0.019$ | ... |
| 12 S8 | $06^h41^m09\overset{s}{.}2$ | $09°33'01''$ | $9.04 \pm 0.51$ | $1.447 \pm 0.019$ | ... |
| 25 NIR | $06^h41^m02\overset{s}{.}6$ | $10°15'02''$ | <2.2 | <0.056 | ... |
| 25 S1 | $06^h41^m03\overset{s}{.}5$ | $10°15'10''$ | $7.1 \pm 2.3$ | $2.92 \pm 0.024$ | ... |
| 25 S2 | $06^h41^m04\overset{s}{.}9$ | $10°14'55''$ | $14.8 \pm 2.3$ | $3.33 \pm 0.024$ | ... |
| 27 S1 | $06^h40^m58\overset{s}{.}5$ | $10°36'54''$ | $31.8 \pm 1.6$ | $3.20 \pm 0.018$ | $0.8 \pm 0.28$ |
| 27 S2 | $06^h40^m59\overset{s}{.}1$ | $10°36'09''$ | $12.1 \pm 1.6$ | $1.87 \pm 0.018$ | $0.7 \pm 0.25$ |
| 27 S3 | $06^h41^m02\overset{s}{.}0$ | $10°35'30''$ | $12.9 \pm 1.6$ | $1.72 \pm 0.018$ | ... |
| 27 S4 | $06^h40^m54\overset{s}{.}4$ | $10°33'27''$ | $7.4 \pm 1.6$ | $0.65 \pm 0.018$ | ... |

The 450- and 850-μm fluxes are integrated over a 45-arcsec aperture. The 1300-μm fluxes represent fluxes within a 27-arcsec beam. The 450- and 850-μm fluxes for RNO and 25 NIR are given as upper limits, since these sources have no corresponding submillimetre peaks.
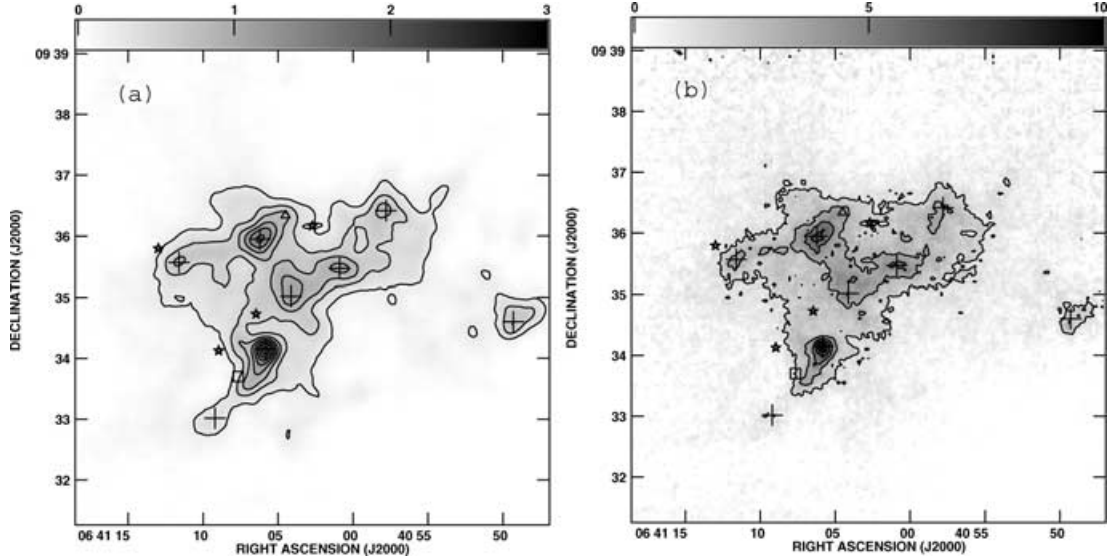
**Figure 1.** Contoured grey-scale images (Jy beam$^{-1}$) of IRAS 12 at: (a) 850 μm, with contours incremented in 0.24 Jy beam$^{-1}$ intervals beginning with 0.24 Jy beam$^{-1}$; and (b) 450 μm, with contours incremented in 1.2 Jy beam$^{-1}$ intervals beginning with 1.2 Jy beam$^{-1}$. Submillimetre sources are marked with crosses (+); the *IRAS* source error ellipse is indicated; the positions of the near-infrared sources are marked with stars; the VLA source is marked with a triangle; and the H$_2$O maser is marked with an open square.

submillimetre sources that were identified in the three regions, the 1.3-mm fluxes that were obtained for a few sources at the former NRAO 12-m telescope on Kitt Peak, and the errors associated with the fluxes.

### 3.2.1 IRAS 06382+0939 (IRAS 12)

Fig. 1(a) shows the 850-μm emission associated with IRAS 12. Near-infrared sources (stars), the VLA source (triangle), the position of an H$_2$0 maser (open square) identified by Mendoza et al. (1990) and the *IRAS* point source error ellipse are indicated. We detected eight compact submillimetre sources (crosses) in the mapped region, which we designate as '12 S#' in this paper. Recently, lower-resolution 870-μm observations of this region resulted in the detection of seven compact sources (Williams & Garland 2002). The map shows extended as well as compact emission, but there is clearly little emission at the position of the *IRAS* source, corresponding to the RNO binary. The source 12 S1 is coincident with the other far-infrared peak reported by Cohen et al. (1985). It is also approximately coincident with the peaks of the CS $J = 2 \rightarrow 1$ and CS $J = 5 \rightarrow 4$ emission reported by WWL95. The overall morphology of the extended 850-μm emission is very similar to the morphology of the CS $J = 5 \rightarrow 4$ emission mapped by WWL95 (see fig. 5b of WWL95). Notably, WWL95 detected no CS $J = 5 \rightarrow 4$ emission at the position of the *IRAS* point source. Fig. 1(b) shows the 450-μm emission associated with IRAS 12. Although significantly noisier than the 850-μm data, all of the submillimetre sources present in the 850-μm map are identifiable at 450 μm as well. The close association of the submillimetre and CS $J = 5 \rightarrow 4$ emission, which traces dense gas of $\sim 10^6$ cm$^{-3}$ (WWL95), and the fact that none of the submillimetre peaks is coincident with any of the near-infrared sources identified by Mendoza et al. (1990), suggest that the submillimetre sources are very young objects, most likely Class 0 sources and/or pre-stellar cores. Similar anticorrelations between infrared and millimetre peaks are seen in other star-forming regions (e.g. Casali, Eiroa & Duncan 1993; Hurt & Barsony

1996), and have been interpreted as reflecting different phases of star formation.

### 3.2.2 IRAS 06382+1017 (IRAS 25)

Fig. 2(a) shows 850-μm emission associated with IRAS 25. The position of the *IRAS* source error ellipse, near-infrared source (star), Herbig–Haro knots HH124 A–F (crosses ×) and two VLA sources (triangles) are indicated. Although the emission is extended, at least two compact peaks can be identified (crosses +). These peaks are also apparent in the 450-μm emission shown in Fig. 2(b). The brighter peak (25 S1) coincides approximately with VLA 2, which lies $\approx 15$ arcsec to the east of VLA 1 (approximately twice the 7-arcsec resolution of our 450-μm SCUBA data). Unlike VLA 1, VLA 2 has no point-source near-infrared counterpart. It lies in a concavity seen at the north-east end of the infrared reflection nebulosity reported by Piché et al. (1995). The slightly fainter SCUBA peak to the south-east of 25 S1 (25 S2) is not associated with any known near-infrared or radio continuum source.

### 3.2.3 IRAS 06381+1039 (IRAS 27)

Fig. 3(a) shows the 850-μm emission associated with IRAS 27. The position of the *IRAS* source error ellipse is indicated. We detected four compact submillimetre sources in the mapped region (crosses +). Three of these sources lie along a filament of extended emission, similar to those seen in many other submillimetre maps of star-forming regions (e.g. Mitchell et al. 2001). Fig. 3(b) shows the 450-μm emission associated with IRAS 27. Although the image is very noisy, we were able to obtain fluxes for all four compact sources.

## 3.3 HIRES maps and models

In this section, we demonstrate that *IRAS* fluxes tend to probe the overall properties of clumps – protostellar groups – rather than the properties of individual protostellar cores. We show that HIRES
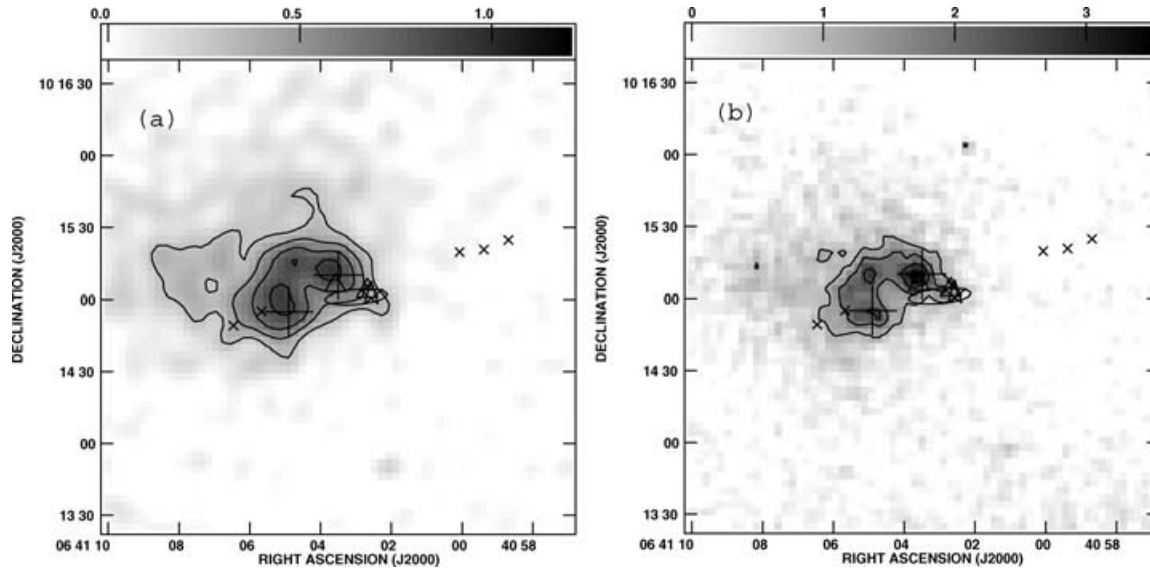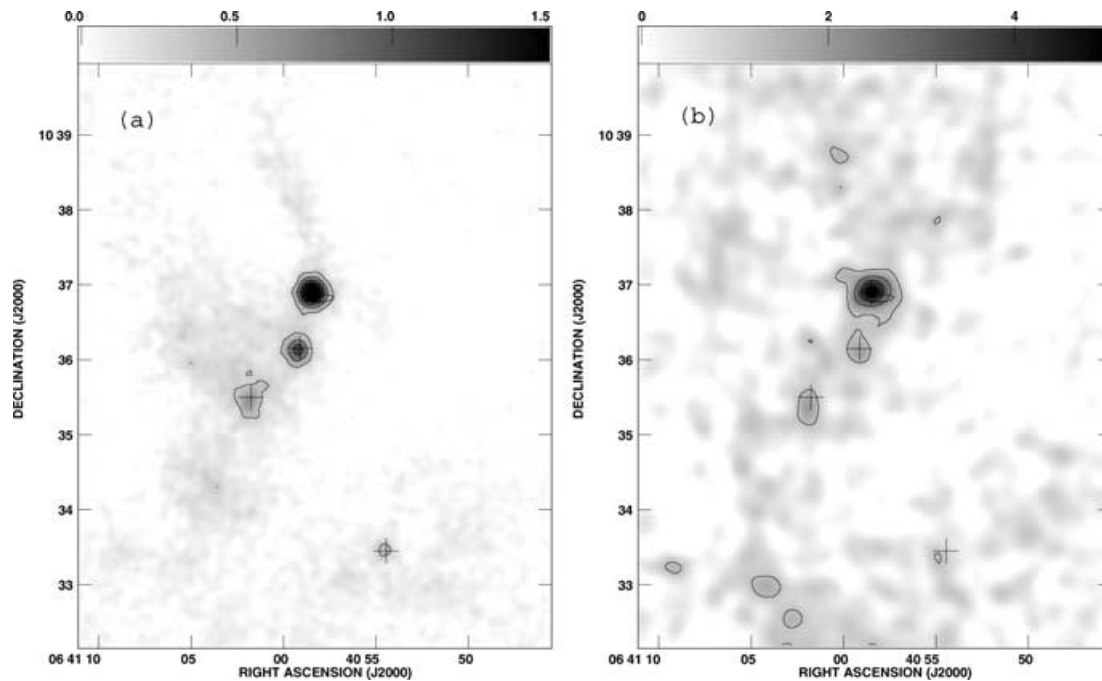
**Figure 2.** Contoured grey-scale images (Jy beam$^{-1}$) of IRAS 25 at: (a) 850 μm, with contours incremented in 0.20 Jy beam$^{-1}$ intervals beginning with 0.30 Jy beam$^{-1}$; and (b) 450 μm, with contours incremented in 0.7 Jy beam$^{-1}$ intervals beginning with 1.1 Jy beam$^{-1}$. Submillimetre sources are marked with crosses (+); the *IRAS* source error ellipse is indicated; the position of the near-infrared source is marked with a star; the VLA sources are marked with triangles; and HH124 A–F are marked with crosses (×).



**Figure 3.** Contoured grey-scale images (Jy beam$^{-1}$) of IRAS 27 at: (a) 850 μm, with contours incremented in 0.32 Jy beam$^{-1}$ intervals beginning with 0.32 Jy beam$^{-1}$; and (b) 450 μm, with contours incremented in 1.2 Jy beam$^{-1}$ intervals beginning with 1.2 Jy beam$^{-1}$. Submillimetre sources are marked with crosses (+); and the *IRAS* source error ellipse is indicated.

point-source models based on the source fluxes and positions given in the *IRAS* Point Source Catalogue are completely inadequate to model the actual emission. Using our SCUBA data to help guide placement and fluxes of input spikes, we construct far more accurate models of the far-infrared emission. Spike positions and fluxes are adjusted until the models most closely match the data in morphology and flux. Figs 4–6 present HIRES maps for the three regions in the following manner: the first row of each figure shows the FRESCO

(full-resolution co-add: equivalent to a single iteration of HIRES) map for each waveband; the second shows HIRES results achieved after 40 iterations for the 12- and 25-μm wavebands, and after 200 iterations for the 60- and 100-μm wavebands; the third row shows point-source models of the HIRES-processed emission using single spikes corresponding to the position and fluxes given in the *IRAS* Point Source Catalogue; and the fourth row shows the final models of the HIRES-processed emission using multiple spikes. No 12-μm

**Table 2.** HIRES model spike positions and fluxes.

| Source | $\alpha$(2000) | $\delta$(2000) | Spike height (Jy) at $\lambda$ | | | | Effective beam size[a] (arcsec) | | | |
|---|---|---|---|---|---|---|---|---|---|---|
| | | | 12 μm | 25 μm | 60 μm | 100 μm | 12 μm | 25 μm | 60 μm | 100 μm |
| RNO | 06ʰ41ᵐ02ˢ8 | 09°36′10″ | 5.5 ± 1.2 | 5.5 ± 1.2 | 91 ± 20 | 135 ± 29 | 47 × 37 | 33 × 29 | 48 × 41 | 51 × 48 |
| | 06ʰ41ᵐ01ˢ7 | 09°36′16″ | . . . | 5.5 ± 1.2 | . . . | . . . | . . . | 33 × 30 | . . . | . . . |
| 12 S1 | 06ʰ41ᵐ05ˢ8 | 09°34′09″ | <0.10 | 0.90 ± 0.19 | 22 ± 5 | 134 ± 29 | 73 × 48 | 52 × 42 | 61 × 47 | 86 × 66 |
| 12 S2 | 06ʰ41ᵐ06ˢ2 | 09°35′57″ | 0.30 ± 0.06 | 1.1 ± 0.2 | 27 ± 6 | 74 ± 16 | 31 × 28 | 31 × 27 | 32 × 30 | 50 × 45 |
| 12 S3 | 06ʰ41ᵐ04ˢ1 | 09°35′01″ | <0.10 | <0.10 | 6.9 ± 1.5 | 39 ± 8 | 32 × 21 | 35 × 31 | 57 × 46 | 33 × 33 |
| 12 S4 | 06ʰ41ᵐ00ˢ9 | 09°35′28″ | 0.50 ± 0.11 | 0.10 ± 0.02 | 28 ± 6 | 161 ± 35 | 33 × 30 | 33 × 29 | 48 × 40 | 49 × 48 |
| 12 S5 | 06ʰ40ᵐ49ˢ3 | 09°34′36″ | <0.10 | 0.10 ± 0.02 | 1.0 ± 0.2 | 0.50 ± 0.11 | 70 × 46 | 42 × 28 | 68 × 31 | 17 × 17 |
| 12 S6 | 06ʰ40ᵐ57ˢ8 | 09°36′25″ | 0.70 ± 0.15 | 0.60 ± 0.13 | 16 ± 3 | 10 ± 2 | 33 × 30 | 31 × 30 | 45 × 42 | 33 × 32 |
| 12 S7 | 06ʰ41ᵐ11ˢ6 | 09°35′34″ | 0.15 ± 0.03 | 1.3 ± 0.3 | 17 ± 4 | 33 ± 7 | 70 × 46 | 55 × 44 | 70 × 49 | 67 × 55 |
| 12 S8 | 06ʰ41ᵐ09ˢ2 | 09°33′01″ | <0.10 | 0.10 ± 0.02 | 1.5 ± 0.3 | 0.40 ± 0.09 | 59 × 49 | 63 × 51 | 39 × 29 | 33 × 31 |
| VLA | 06ʰ41ᵐ04ˢ5 | 09°36′20″ | . . . | . . . | 16 ± 3 | 25 ± 5 | . . . | . . . | 32 × 31 | 33 × 32 |
| IRS A | 06ʰ41ᵐ06ˢ5 | 09°34′44″ | . . . | 1.5 ± 0.3 | . . . | . . . | . . . | 78 × 63 | . . . | . . . |
| IRS F | 06ʰ41ᵐ09ˢ0 | 09°34′08″ | . . . | 0.70 ± 0.15 | . . . | . . . | . . . | 50 × 43 | . . . | . . . |
| | 06ʰ41ᵐ01ˢ1 | 09°36′55″ | 0.40 ± 0.09 | 1.0 ± 0.2 | 20 ± 4 | 100 ± 22 | 34 × 22 | 33 × 22 | 32 × 27 | 50 × 46 |
| | 06ʰ41ᵐ01ˢ6 | 09°35′49″ | 2.0 ± 0.4 | 3.2 ± 0.7 | . . . | . . . | 49 × 39 | 33 × 27 | . . . | . . . |
| 25 NIR | 06ʰ41ᵐ02ˢ6 | 10°15′02″ | 0.52 ± 0.11 | 5.2 ± 1.1 | 18 ± 4 | 14 ± 3 | 51 × 39 | 46 × 29 | 32 × 31 | 51 × 47 |
| 25 S1 | 06ʰ41ᵐ03ˢ5 | 10°15′10″ | 0.17 ± 0.04 | 1.9 ± 0.4 | 9.5 ± 2.0 | 22 ± 5 | 33 × 27 | 32 × 26 | 32 × 28 | 51 × 47 |
| 25 S2 | 06ʰ41ᵐ04ˢ9 | 10°14′55″ | 0.30 ± 0.06 | 1.1 ± 0.2 | 8.5 ± 1.8 | 28 ± 6 | 32 × 30 | 29 × 28 | 31 × 30 | 50 × 47 |
| | 06ʰ41ᵐ03ˢ6 | 10°14′34″ | 0.29 ± 0.06 | . . . | 8.0 ± 1.7 | . . . | 50 × 37 | . . . | 32 × 27 | . . . |
| 27 S1 | 06ʰ40ᵐ58ˢ5 | 10°36′54″ | 0.25 ± 0.05 | 2.5 ± 0.5 | 35 ± 8 | 73 ± 16 | 56 × 42 | 55 × 31 | 32 × 31 | 50 × 48 |
| | 06ʰ40ᵐ59ˢ0 | 10°37′04″ | . . . | . . . | 18 ± 4 | . . . | . . . | . . . | 32 × 29 | . . . |
| | 06ʰ40ᵐ58ˢ0 | 10°37′04″ | . . . | . . . | . . . | 58 ± 12 | . . . | . . . | . . . | 50 × 47 |
| 27 S2 | 06ʰ40ᵐ59ˢ1 | 10°36′09″ | <0.10 | <0.10 | 7.0 ± 1.5 | 13 ± 3 | 56 × 45 | 33 × 31 | 44 × 41 | 33 × 32 |
| 27 S3 | 06ʰ41ᵐ02ˢ0 | 10°35′30″ | <0.10 | 0.10 ± 0.02 | 1.2 ± 0.3 | <0.10 | 72 × 43 | 74 × 50 | 59 × 38 | 32 × 27 |
| 27 S4 | 06ʰ40ᵐ54ˢ4 | 10°33′27″ | <0.10 | <0.10 | 1.2 ± 0.3 | 0.33 ± 0.07 | 60 × 43 | 50 × 41 | 65 × 41 | 51 × 45 |
| | 06ʰ41ᵐ02ˢ8 | 10°35′01″ | . . . | . . . | 1.2 ± 0.3 | . . . | . . . | . . . | 52 × 40 | . . . |

[a]Effective beam size is shown as major × minor axes.

maps are shown for IRAS 27, which was marginally detected at the PSC position. The most striking differences between the HIRES PSC and multiple spike models are seen for IRAS 12, where objects contained within the *IRAS* source are spread over a larger region than objects contained within the other *IRAS* sources (Fig. 4).

Table 2 lists the final positions and magnitudes of HIRES model input spikes that were used for the relevant wavebands, and the resolutions achieved at these positions. The associated errors are computed from the ~20 per cent error inherent in HIRES (Levine & Surace 1993) in combination with the error associated with the point-source models, which we estimate to be <8 per cent. This is the maximum amount that the input fluxes can vary without causing significant changes in the resulting models. We note that in all of the modelled regions it was necessary to add additional spikes in at least one of the wavebands that are not coincident with any known sources in order to closely simulate the observed emission. We interpret this as being due to the presence of extended dust emission in these regions, as is clearly seen in the SCUBA maps. We emphasize that the HIRES-derived source fluxes should therefore be interpreted as upper limits to the actual source fluxes. Additionally, many of the submillimetre sources were only weakly detected at 12 and 25 μm. HIRES processing is, in general, unreliable for unresolved sources significantly fainter than 1 Jy (Levine & Surace 1993).

The most accurate set of HIRES fluxes was derived for 12 S1 due to the brightness of this object and its relative isolation from other nearby objects. It was possible to model the HIRES-processed emission extremely closely with a single spike located at the submillimetre source position. We present the SED and derived properties

for this object in Section 3.5. We note here that the Two-Micron All Sky Survey (2MASS) Point Source Catalogue (PSC) has been released since completion of this work. Six of the submillimetre sources presented in this paper have one or more faint near-infrared counterparts. We will present SEDs and a more detailed analysis of these sources in a subsequent paper.

### 3.3.1 IRAS 06382+0939 (IRAS 12)

Fig. 4 presents HIRES maps and models of the four *IRAS* wavebands for IRAS 12. Very little structure is present in all of the FRESCO maps (Figs 4a–d); however, the HIRES-processed maps (Figs 4e–h) clearly indicate that not all of the emission comes from *IRAS* 06382+0939: the 12-μm map shows a clear extension towards 12 S6; the 25- and 60-μm maps show additional extensions towards 12 S7 and separate peaks at 12 S1; and the 100-μm map shows a pronounced extension towards 12 S1. Comparing these maps to models based on Point Source Catalogue positions and fluxes (Figs 4i–l) illustrates the inadequacy of these models to reproduce the actual emission. For the models shown in Figs 4(m)–(p), spikes were used at the submillimetre source positions, the *IRAS* point source position, and various other positions that either correspond to other known sources, or simply help simulate extended emission.

### 3.3.2 IRAS 06382+1017 (IRAS 25)

Fig. 5 presents HIRES maps and models of the four *IRAS* wavebands for IRAS 25. Once again, very little structure is seen in
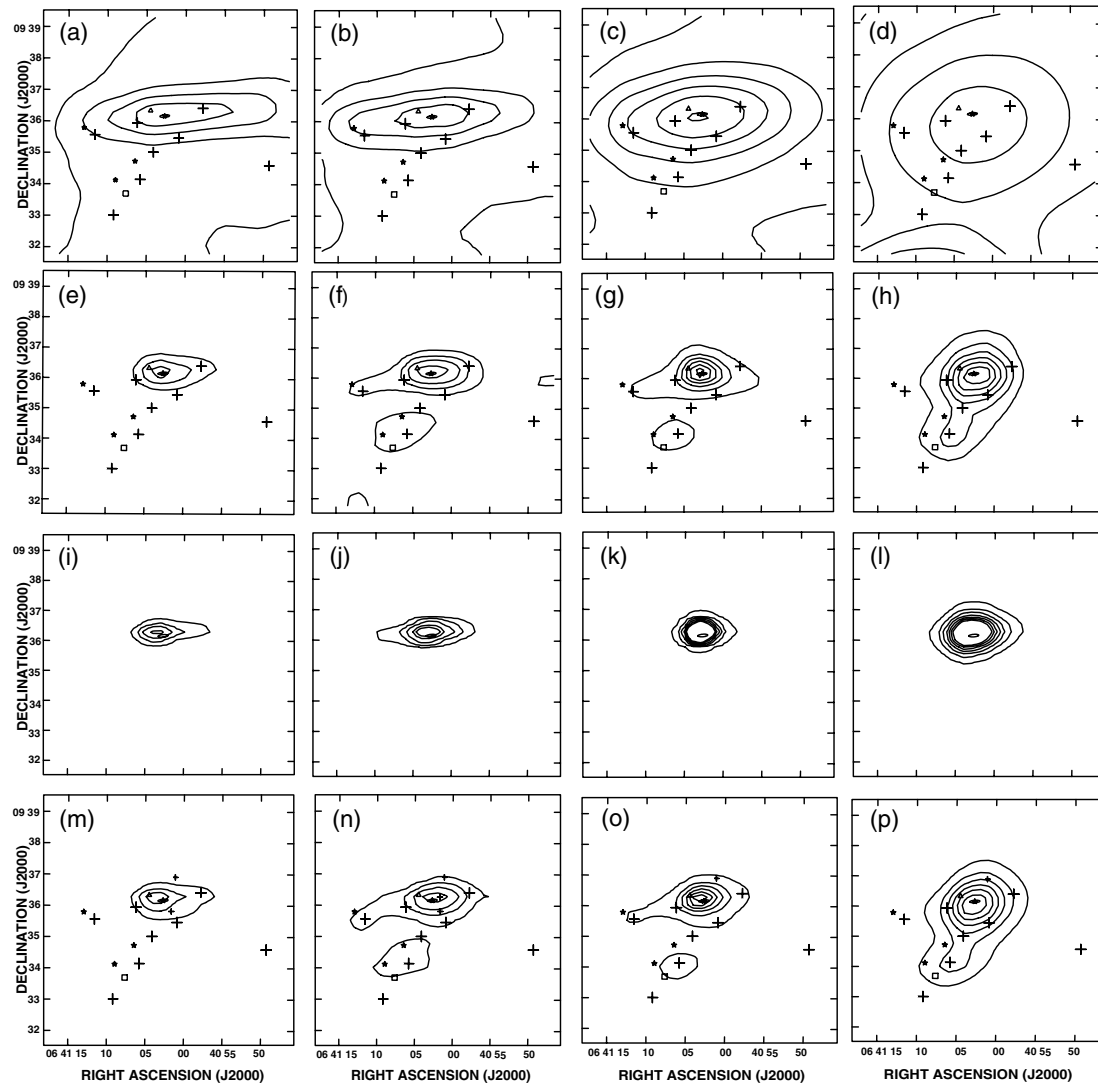
**Figure 4.** (*top row*) IRAS 12 HIRES-processed emission after one iteration at (a) 12 μm (contour levels 5, 10, 15, 20 MJy sr$^{-1}$), (b) 25 μm (contour levels 10, 20, 30, 40 MJy sr$^{-1}$), (c) 60 μm (contour levels 50, 100, 150, 200, 250, 300 MJy sr$^{-1}$) and (d) 100 μm (contour levels 100, 200, 300, 400 MJy sr$^{-1}$). (*second row*) IRAS 12 HIRES-processed emission after 40 iterations at (e) 12 μm (contour levels 20, 50, 100 MJy sr$^{-1}$) and (f) 25 μm (contour levels 20, 50, 100, 200 MJy sr$^{-1}$), and after 200 iterations at (g) 60 μm (contour levels 200, 600, $1 \times 10^3$, $1.4 \times 10^3$, $1.8 \times 10^3$, $2.2 \times 10^3$ MJy sr$^{-1}$) and (h) 100 μm (contour levels 400, 800, $1.2 \times 10^3$, $1.6 \times 10^3$, $2.0 \times 10^3$, $2.4 \times 10^3$, $2.8 \times 10^3$ MJy sr$^{-1}$). (*third row*) HIRES-processed models using PSC positions and fluxes after 40 iterations at (i) 12 μm (contour levels same as (e)) and (j) 25 μm (contour levels same as (f)), and after 200 iterations at (k) 60 μm (contour levels same as (g)) and (l) 100 μm (contour levels same as (h)). (*bottom row*) Multi-spike HIRES-processed models after 40 iterations at (m) 12 μm (contour levels same as (e)) and (n) 25 μm (contour levels same as (f)), and after 200 iterations at (o) 60 μm (contour levels same as (g)) and (p) 100 μm (contour levels same as (h)). Source symbols are as follows: *IRAS* source position (ellipse); near-infrared sources (stars); submillimetre sources (large crosses +); VLA source (triangle); and H$_2$O maser (open square). Small crosses (+) mark the position of spikes not corresponding to any known sources that were used to simulate the emission more accurately.

the FRESCO maps (Figs 5a–d), except for a pronounced shift to the north-east in the peak of the 100-μm emission. The HIRES-processed *IRAS* emission (Figs 5e–h) is well peaked on the *IRAS* source at 25 and 60 μm, but the 100-μm emission clearly shows the peak to be closer to the centre of 25 S1 and 25 S2. Models based on Point Source Catalogue positions and fluxes (Figs 5i–l) fail to reproduce the actual emission, particularly at 100 μm. Figs 5(m)–(p) are HIRES models using spikes at the submillimetre sources positions and the near-infrared source position (coincident with the *IRAS* point source). An additional spike at no known source position was required to model the 12- and 60-μm emission more accurately.

### 3.3.3 IRAS 06381+1039 (IRAS 27)

Fig. 6 presents HIRES maps and models of the 25-, 60- and 100-μm wavebands for IRAS 27. Since 27 S1 was marginally detected at 12 μm and the other sources are non-detections, we do not include these maps. There is little structure in the FRESCO maps (Figs 6a–c). While the HIRES-processed emission is peaked at the *IRAS* source position in all wavebands (Figs 6d–f), the 60-μm map shows a clear extension along the arc formed by 27 S1, 27 S2 and 27 S3, and a separate, albeit weak, peak appears close to the position of 27 S4. The Point Source Catalogue models (Figs 6g–i) do not adequately reproduce this emission. More
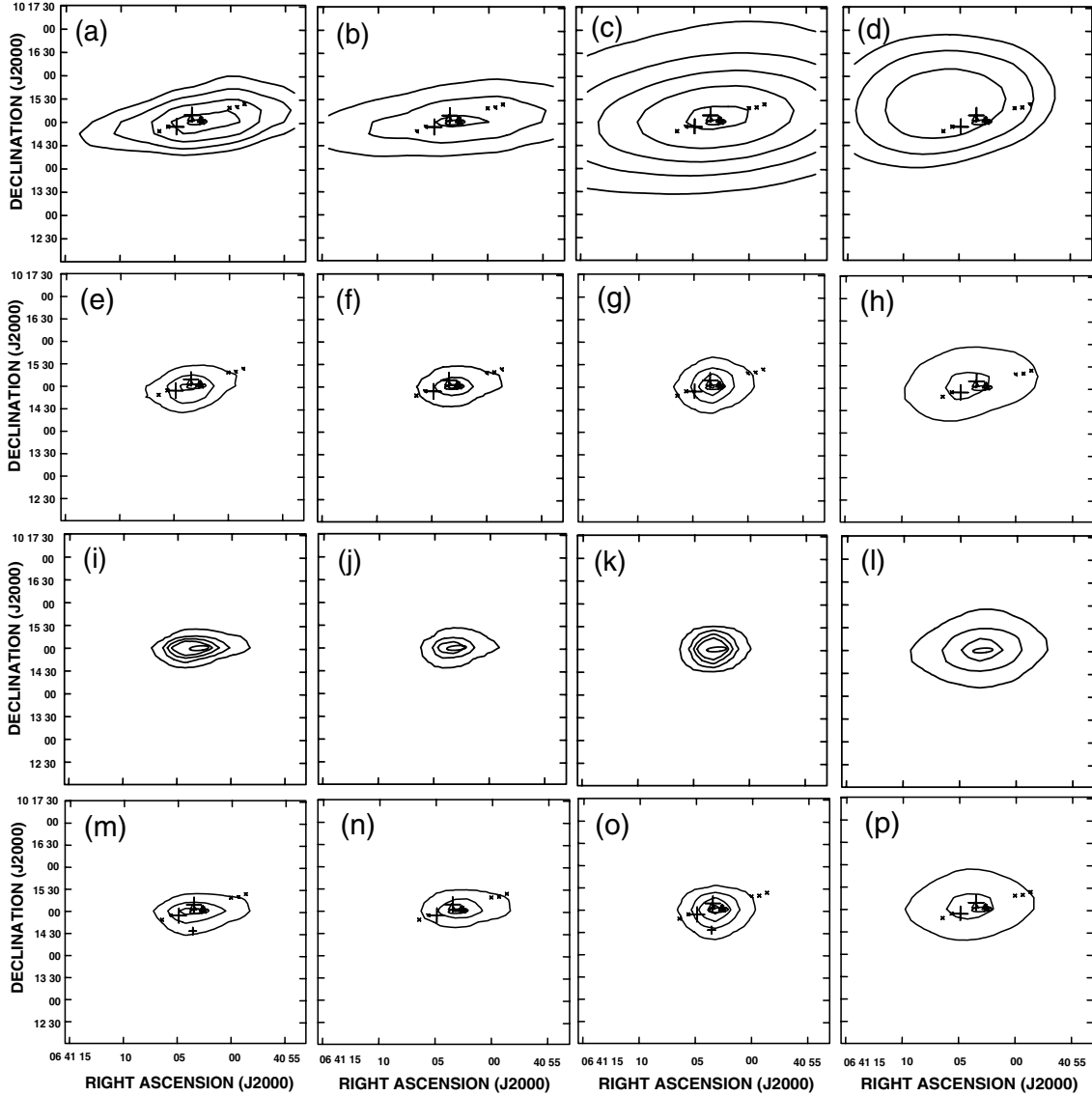
**Figure 5.** (*top row*) IRAS 25 HIRES-processed emission after one iteration at (a) 12 μm (contour levels 2, 2.5, 3, 3.5 MJy sr$^{-1}$), (b) 25 μm (contour levels 5, 10, 15 MJy sr$^{-1}$), (c) 60 μm (contour levels 10, 20, 30, 40, 50 MJy sr$^{-1}$) and (d) 100 μm (contour levels 10, 15, 20 MJy sr$^{-1}$). (*second row*) IRAS 25 HIRES-processed emission after 40 iterations at (e) 12 μm (contour levels 5, 10, 15, 20 MJy sr$^{-1}$) and (f) 25 μm (contour levels 20, 100, 200 MJy sr$^{-1}$), and after 200 iterations at (g) 60 μm (contour levels 100, 300, 500, 700 MJy sr$^{-1}$) and (h) 100 μm (contour levels 100, 300, 500 MJy sr$^{-1}$). (*third row*) HIRES-processed models using PSC positions and fluxes after 40 iterations at (i) 12 μm (contour levels same as (e)) and (j) 25 μm (contour levels same as (f)), and after 200 iterations at (k) 60 μm (contour levels same as (g)) and (l) 100 μm (contour levels same as (h)). (*bottom row*) Multi-spike HIRES-processed models after 40 iterations at (m) 12 μm (contour levels same as (e)) and (n) 25 μm (contour levels same as (f)), and after 200 iterations at (o) 60 μm (contour levels same as (g)) and (p) 100 μm (contour levels same as (h)). Source symbols are as follows: *IRAS* source position (ellipse); near-infrared source (star); submillimetre sources (large crosses +); VLA sources (triangles); and Herbig–Haro objects (crosses ×). The small cross (+) in the 12- and 60-μm maps marks the position of a spike not corresponding to any known source that was used to simulate the emission more accurately.

accurate models (Figs 6j–l) use spikes at the positions of the submillimetre sources, as well as multiple spikes in the immediate vicinity of 27 S1, and an additional spike along the extended ridge of 60-μm emission.

### 3.4 CO outflow maps

In this section, we present CO $J = 2 \rightarrow 1$ maps of outflows associated with the regions containing IRAS 12, 25 and 27. A single outflow has been previously associated with each *IRAS* source (NGC 2264 D, 2264 O and 2264 H), based on CO $J = 1 \rightarrow 0$ and

CS $J = 2 \rightarrow 1$ maps at half the resolution of the maps we present here (MLS88; WW95). Our maps indicate far more complex outflow morphology, and suggest there are multiple outflows in each region.

#### 3.4.1 IRAS 06382+0939 (IRAS 12)

Fig. 7 shows blue- and redshifted high-velocity CO $J = 2 \rightarrow 1$ emission associated with outflow NGC 2264 D (contours) superimposed on the SCUBA 850-μm image (grey-scale). Submillimetre sources (crosses +), H$_2$O maser (open square), VLA source
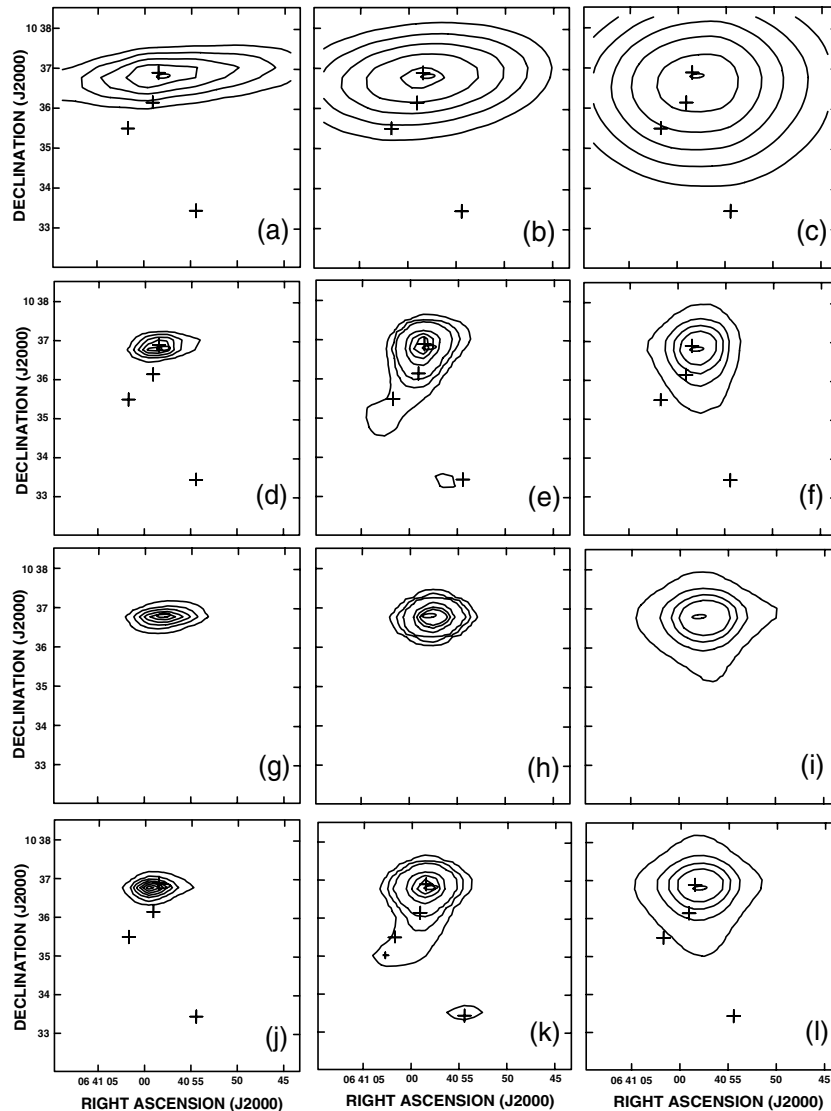
**Figure 6.** (*top row*) IRAS 27 HIRES-processed emission after one iteration at (a) 25 μm (contour levels 2, 3, 4, 5 MJy sr$^{-1}$), (b) 60 μm (contour levels 20, 30, 40, 50, 60 MJy sr$^{-1}$) and (c) 100 μm (contour levels 30, 40, 50, 60, 70 MJy sr$^{-1}$). (*second row*) IRAS 27 HIRES-processed emission after 40 iterations at (d) 25 μm (contour levels 10, 20, 30, 40, 50, 60, 70 MJy sr$^{-1}$), and after 200 iterations at (e) 60 μm (contour levels 20, 50, 100, 400, 700, $1 \times 10^3$ MJy sr$^{-1}$) and (f) 100 μm (contour levels 100, 300, 500, 700 MJy sr$^{-1}$). (*third row*) HIRES-processed models using PSC positions and fluxes after 40 iterations at (g) 25 μm (contour levels same as (d)), and after 200 iterations at (h) 60 μm (contour levels same as (e)) and (i) 100 μm (contour levels same as (f)). (*bottom row*) Multi-spike HIRES-processed models after 40 iterations at (j) 25 μm (contour levels same as (d)), and after 200 iterations at (k) 60 μm (contour levels same as (e)) and (l) 100 μm (contour levels same as (f)). Source symbols are as follows: *IRAS* source position (ellipse); and submillimetre sources (large crosses +). Small crosses (+) mark the position of spikes not corresponding to any known sources that were used to simulate the emission more accurately.

(triangle), near-infrared sources (stars) and the *IRAS* error ellipse are indicated. It is clear that the *IRAS* point source, associated with the RNO binary, is not associated with the high-velocity CO emission. Unfortunately, we cannot unambiguously discern whether the submillimetre source, 12 S1, or the near-infrared source (IRS A) identified by Mendoza et al. (1990), is the principal contributor to the outflow(s). The major portions of the blue- and redshifted lobes appear to lie at different position angles. The blue lobe does not show a well-defined position angle. The major component of the blueshifted emission extends almost due north from the near-infrared source IRS F (Mendoza et al. 1990); to the north-east of this component lies a finger of emission that points back towards 12 S1, along a PA $\sim 33°$. The major component of the redshifted emission lies roughly along PA $\sim 80°$, although a small finger of redshifted

emission extends just south-west of 12 S1 along a position angle similar to the finger of blueshifted emission. Clearly, more sensitive and higher-resolution observations are needed to sort out possible contributions from the various sources in this region, but there is no apparent CO outflow associated with the *IRAS* point source.

### 3.4.2 *IRAS 06382+1017 (IRAS 25)*

Fig. 8 shows blue- and redshifted CO $J = 2 \rightarrow 1$ emission associated with outflow NGC 2264 O (contours) superimposed on the SCUBA 850-μm image (grey-scale). Submillimetre sources (crosses +), VLA sources (triangles), near-infrared source (star), HH124 A–F (crosses ×) and the *IRAS* source error ellipse are indicated. Piché et al. (1995) suggested the possibility of two outflows in this region:
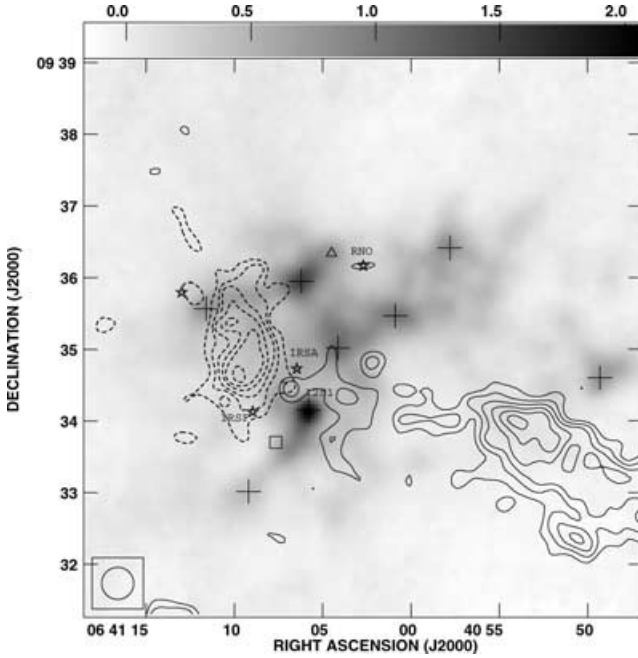
**Figure 7.** Blueshifted (dashed contours) and redshifted (solid contours) CO $J = 2 \rightarrow 1$ emission associated with outflow NGC 2264 D superimposed on the SCUBA 850-μm image (grey-scale: Jy beam$^{-1}$) of IRAS 12. The blueshifted emission has been integrated from $-12.2$ to 1.5 km s$^{-1}$ and is plotted in 10 per cent increments from 45 to 95 per cent of the 31.2 K km s$^{-1}$ emission peak. The redshifted emission has been integrated from 10.6 to 21.3 km s$^{-1}$ and is plotted in 10 per cent increments from 45 to 95 per cent of the 25.6 K km s$^{-1}$ emission peak. Submillimetre sources (crosses $+$), H$_2$O maser (open square), VLA source (triangle), near-infrared sources (stars) identified by Mendoza et al. (1990), and the *IRAS* error ellipse are indicated. Sources explicitly referred to in the text are labelled. The beam size for the CO observations is indicated in the lower left corner.
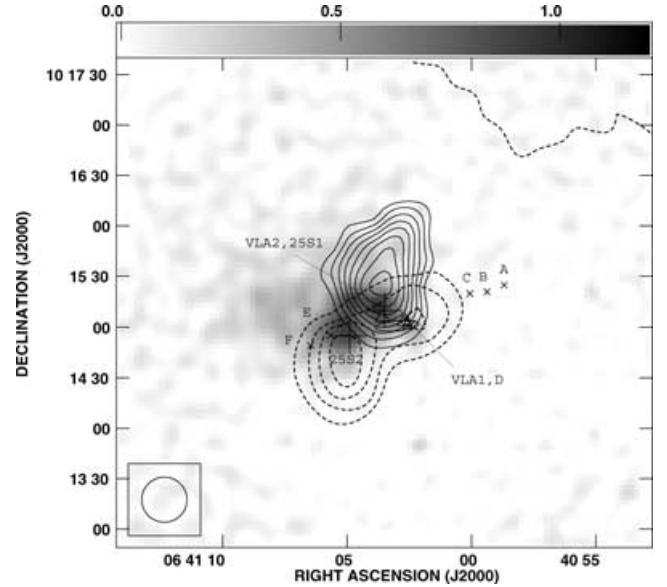


**Figure 8.** Blueshifted (dashed contours) and redshifted (solid contours) CO $J = 2 \rightarrow 1$ emission associated with outflow NGC 2264 O superimposed on the SCUBA 850-μm image (grey-scale: Jy beam$^{-1}$) of IRAS 25. The blueshifted emission has been integrated from $-0.2$ to 4.9 km s$^{-1}$ and is plotted in 10 per cent increments from 60 to 90 per cent of the 23.8 K km s$^{-1}$ emission peak. The redshifted emission has been integrated from 11.1 to 19.2 km s$^{-1}$ and is plotted in 10 per cent increments from 25 to 95 per cent of the 9.8 K km s$^{-1}$ emission peak. Submillimetre sources (crosses $+$), VLA sources (triangles), near-infrared source (star) identified by Piché et al. (1995), HH124 A–F (crosses $\times$), and the *IRAS* source error ellipse are indicated. Sources explicitly referred to in the text are labelled. The beam size for the CO observations is indicated in the lower left corner.

one associated with HH124, lying nearly E–W; and another associated with a wider-angle reflection nebula along a PA = 45°. Our observations indicate three peaks in the high-velocity CO emission: one peak in the redshifted emission, and two peaks in the blueshifted emission. The western blueshifted lobe may be associated with VLA 1 (coincident with the *IRAS* source) and the E–W Herbig–Haro flow, or it may be associated with 25 S1 and the redshifted lobe to the north of 25 S1. The south-eastern blue lobe is probably not associated with the Herbig–Haro flow, since the eastern HH knot E is redshifted, while western knots A–D are strongly blueshifted (Walsh et al. 1992). It may be associated with 25 S2. In any case, the eastern blue lobe does not appear to be related to either of the previously reported outflows, which suggests that there are at least three outflows in the region. Given the compactness of the outflows, it is not possible to associate outflows unambiguously with sources at our resolution.

### 3.4.3 IRAS 06381+1039 (IRAS 27)

Fig. 9 shows blue- and redshifted CO $J = 2 \rightarrow 1$ emission associated with outflow NGC 2264 H (contours) superimposed on the SCUBA 850-μm image (grey-scale). Submillimetre sources (crosses $+$) and the *IRAS* error ellipse are indicated. The high-velocity gas has a very complex morphology, but our map helps to elucidate the 'squat' appearance of this outflow in the MLS88 CO $J = 1 \rightarrow 0$ map, where the 'major' axis of the outflow was reported to be shorter than the

axis perpendicular to the outflow. MLS88 identified this as a single outflow oriented in a north–south direction, but our map indicates that the double-lobed redshifted emission lies east of 27 S1, along PA $\sim$ 113°, and is probably associated with this source (which is also coincident with the *IRAS* source). The small blue lobe directly to the north-west of 27 S1 is probably part of this outflow, although the morphology, as well as the velocity structure, of the blue- and redshifted gas are very different.

The origin of the blueshifted gas to the north-east of 27 S1 is unclear, but may be elucidated in Fig. 10, which shows blueshifted emission integrated from 0.0 to 1.5 km s$^{-1}$ (just outside of the line core emission) and redshifted emission integrated from 8.5 to 10.0 km s$^{-1}$ (just inside the line core), and hence contaminated by ambient emission. Nevertheless, the extended redshifted gas to the south-west and the blueshifted gas to the north-east are roughly bipolar about 27 S2 at a PA = 35°, suggesting that this source may power an outflow along this direction. The 'finger' of blueshifted emission extending north-east from 27 S2 lends support to this interpretation. The blueshifted gas directly north-east of 27 S3 may be associated with this source, but the emission is fairly weak and there is no strong evidence for redshifted gas on the opposite side of 27 S3. In any case, the apparent reason for the 'squat' appearance of NGC 2264 H in the lower-resolution CO $J = 1 \rightarrow 0$ maps (MLS88) is the presence of at least two overlapping outflows in this region. It is interesting to note that the outflows are approximately perpendicular to the curved ridge of submillimetre emission that connects 27 S1, 27 S2 and 27 S3.
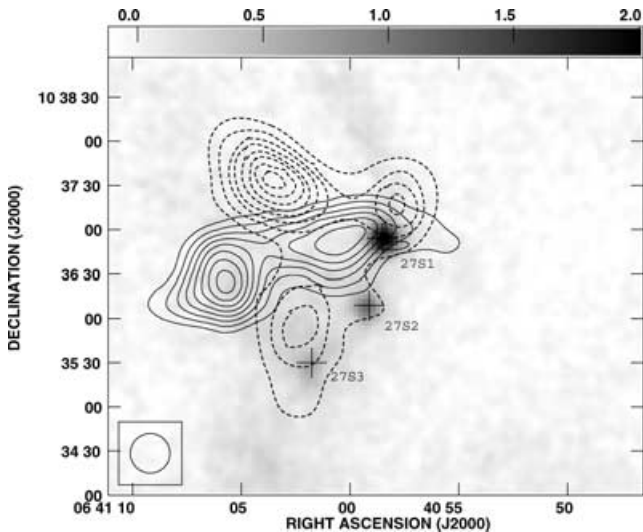
**Figure 9.** Blueshifted (dashed contours) and redshifted (solid contours) CO $J = 2 \to 1$ emission associated with outflow NGC 2264 H superimposed on the SCUBA 850-$\mu$m image (grey-scale: Jy beam$^{-1}$) of IRAS 27. Blueshifted emission from 0.0 to 3.0 km s$^{-1}$ is plotted as contour levels in 10 per cent increments from 25 to 95 per cent of the 12.7 K km s$^{-1}$ emission peak. Redshifted emission from 10.0 to 30.0 km s$^{-1}$ is plotted as contour levels in 10 per cent increments from 25 to 95 per cent of the 37.7 K km s$^{-1}$ emission peak. Submillimetre sources (crosses +) and the *IRAS* error ellipse are indicated. Sources explicitly referred to in the text are labelled. The beam size for the CO observations is indicated in the lower left corner.
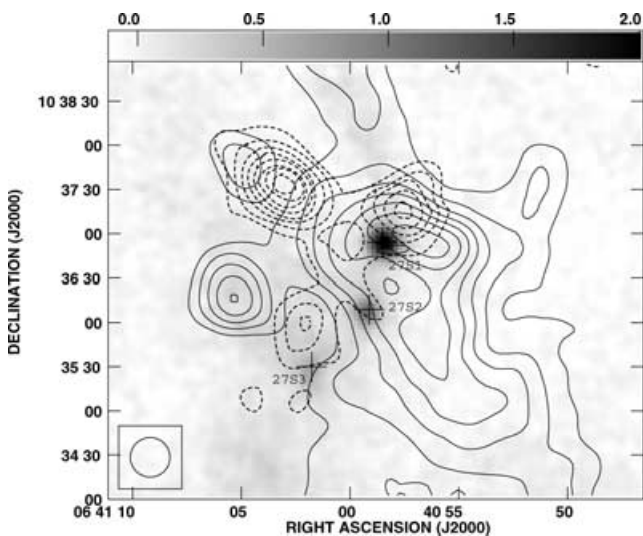


**Figure 10.** Integrated emission from 0.0 to 1.5 km s$^{-1}$ is plotted (dashed contours) in 10 per cent increments from 20 to 90 per cent of the 9.6 K km s$^{-1}$ emission peak. Integrated emission from 8.5 to 10.0 km s$^{-1}$ is plotted (solid contours) in 10 per cent increments from 35 to 95 per cent of the 28.6 K km s$^{-1}$ emission peak. Submillimetre sources (crosses +) and the *IRAS* error ellipse are indicated. Sources explicitly referred to in the text are labelled. The beam size for the CO observations is indicated in the lower left corner.

### 3.5 IRAS 12 S1: an intermediate-mass Class 0 object

As discussed in Section 3.3, IRAS 12 S1 is the only source that could closely be modelled with a single spike in all *IRAS* wavebands, with good spatial separation from other sources. With the combined HIRES, SCUBA and millimetre fluxes, it is possible to plot a SED
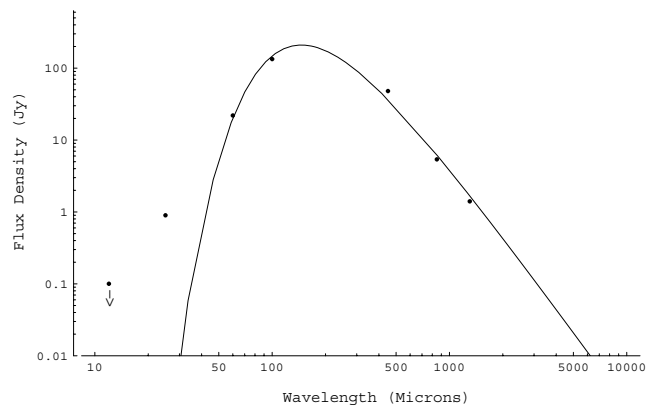


**Figure 11.** SED of IRAS 12 S1: Plotted fluxes are presented in Tables 1 and 2. Parameters of the plotted fit are presented in Table 3.

**Table 3.** IRAS 12 S1 source properties.

| Parameter | Symbol [units] | Value |
|---|---|---|
| IRAS 12 S1 RA | $\alpha(2000)$ | $06^{h}41^{m}05\overset{s}{.}8$ |
| IRAS 12 S1 Dec. | $\delta(2000)$ | $09°34'09''$ |
| Adopted distance | $D$ [pc] | 800 |
| Fitted temperature | $T_d$ [K] | 23 |
| Fitted optical depth | $\tau_{250\,\mu m}$ | 0.04 |
| Fitted source diameter | d$\Omega$ [arcsec] | 28 |
| Bolometric luminosity | $L_{bol}$ [L$_\odot$] | 107.5 |
| | $L_{submm}/L_{bol}$ | 0.03 |
| Circumstellar envelope mass | $M_{env}$ [M$_\odot$] | 17.6 |

The adopted distance, originally estimated by Walker (1956), is the same distance as adopted for the surveys of MLS88 and MLY89, which are discussed in the text.

with several reliable flux points on both the Wien and Rayleigh–Jeans sides of the peak to help constrain physical parameters of this object. Fig. 11 displays this SED, along with a single-temperature, modified blackbody fit of the form

$$S_\nu = B_\nu(T_d)(1 - e^{-\tau_\nu})\,d\Omega. \qquad (1)$$

The best fit was derived using a $\nu^{1.4}$ wavelength dependence of the dust optical depth. The best-fitting source diameter d$\Omega$, dust temperature $T_d$, and 250-$\mu$m optical depth are listed in Table 3. The source properties that can be derived from the model fit, such as the source bolometric luminosity $L_{bol}$, and the circumstellar mass $M_{env}$, are also listed in Table 3, and were derived in a manner analogous to that described in Barsony et al. (1998) for other Class 0 sources. The tabulated bolometric luminosity was derived by numerical integration under the fitted curve plotted in Fig. 11.

Class 0 objects have ratios of $L_{submm}/L_{bol} \geqslant 5 \times 10^{-3}$, where $L_{submm}$ is the luminosity radiated longward of 350 $\mu$m (André, Ward-Thompson & Barsony 1993). The derived ratio of $L_{submm}/L_{bol} = 0.03$ for IRAS 12 S1 places this object well within the Class 0 category. Additionally, if IRAS 12 S1 is the main contributor to out-flow NGC 2264 D, then its outflow momentum flux ($1.3 \times 10^{-3} \leqslant F_{CO}/M_\odot$ km s$^{-1}$ yr$^{-1} \leqslant 7.5 \times 10^{-3}$; MLS88) is roughly an order of magnitude greater than expected for a Class I object of comparable bolometric luminosity, which is typical for Class 0 objects (see e.g. fig. 5 in Bontemps et al. 1996). The computed parameters suggest that IRAS 12 S1 comprises one or more intermediate-mass protostars.

As stated in Section 3.3, the recently released 2MASS PSC indicates that six of the submillimetre sources discussed in this paper have near-infrared counterparts. IRAS 12 S1 has three faint near-infrared counterparts that lie within a 7 arcsec radius of the SCUBA position. Although lack of detection in the near-infrared has generally been used as a criterion for Class 0 status, we note that eight of the 42 confirmed Class 0 objects listed in table 1 of André, Ward-Thompson & Barsony (2000) can also be associated with 2MASS point sources that lie within 7 arcsec of these objects: W3OH-TW, L1448-N(A), L1641-VLA1, HH24MMS, IRAS 08076, L483-MM, G 34.24+0.13MM and S106-SMM. Of these, W3OH-TW and G 34.24+0.13MM are candidate massive Class 0 objects, and L1641-VLA1, IRAS 08076 and L483-MM are listed as borderline Class 0 objects (André et al. 2000). L1448-N(A) has recently been suggested to be a borderline Class 0 object by O'Linger et al. (2003), who argue that lack of detection shortward of 10 μm should be discarded as a criterion for Class 0 status, since this characteristic reflects current technology rather than intrinsic source properties.

## 4 DISCUSSION

It is important to ascertain which sources within clumps drive molecular outflows and/or jets in order to investigate similarities and differences between low- and high-mass YSOs that are associated with these phenomena, and to correlate accurately sources and outflow parameters. Our new observations and modelling indicate that previously categorized 'Class I objects' in the Mon OB1 dark cloud are, in fact, associated with protoclusters containing multiple sources at different evolutionary stages. In two cases, the object identified as the 'IRAS point source' is undetected at submillimetre wavelengths, but lies near multiple submillimetre sources. In both cases, the submillimetre sources contribute significantly to the IRAS fluxes at 60 and 100 μm, but the IRAS source dominates at shorter wavelengths.

Correlations between outflow force or momentum deposition rate, $F_{CO}$, and source luminosity, $L_{bol}$, have been noted over many decades of luminosity since the earliest surveys for outflows (e.g. Bally & Lada 1983; Panagia 1991; Cabrit & Bertout 1992). Many of these correlations were established by making extensive use of the IRAS data base to help establish source luminosities. Furthermore, the $F_{CO}/L_{bol}$ ratio has been used to estimate the fraction of the accretion flow that is ejected in the wind, in order to help distinguish between different models of the wind ejection mechanism (e.g. Richer et al. 2000). Our results suggest that many of the noted source–outflow correlations may reflect the sum total of source and outflow properties from a protocluster or protogroup rather than the properties of individual sources within the cluster. Hence, the relationship between outflow momentum and source bolometric luminosity at high source luminosities is particularly called into question.

To investigate the effect of our results on the previously calculated IRAS luminosities for the sources in this study, we note that MLY89 calculated IRAS luminosities for the Mon OB1 sources IRAS 12, 25 and 27 to be 330, 110 and 87 $L_{\odot}$, respectively. Applying MLY89's equation (1) to the IRAS upper limits we derived for the 'point sources', we find the luminosities for IRAS 12 (RNO), IRAS 25 (NIR) and IRAS 27 (27 S1) to be 150, 28 and 74 $L_{\odot}$, respectively. For the first two cases the recalculated luminosities are significantly lower than the original calculations. Calculated in this manner, the IRAS luminosity of the source that we identify as a likely contributor to NGC 2264 D, 12 S1, is only ~48 $L_{\odot}$; however, the bulk of the luminosity from this source is emitted at longer wavelengths and our calculated bolometric luminosity is 107.5 $L_{\odot}$.

Our results indicate that extreme care must be taken when using outflow momentum deposition rates and source luminosities in order to infer the relationship between accretion rates and outflow. Outflow momentum deposition rates cannot be unequivocally correlated with source luminosities in many of the clustered regions for which these luminosities were derived from IRAS fluxes. The similar resolving ability of the Stratospheric Observatory for Infrared Astronomy (SOFIA) at infrared wavelengths to the JCMT's SCUBA at submillimetre wavelengths, combined with higher-resolution outflow observations, should enable a critical assessment of the properties of outflows and driving sources in many clustered regions.

## 5 SUMMARY

We have used HIRES processing and modelling of IRAS data, along with SCUBA imaging, to identify individual cores embedded in massive CS clumps in the Mon OB1 dark cloud, and estimate their contributions to the IRAS fluxes. Each CS clump had been previously associated with a single IRAS point source. The associated YSO was, in each case, linked with a single molecular outflow and had been assigned a Class I type SED. In two of the three clumps studied, none of the bright submillimetre sources is coincident with the identified IRAS 'point source'.

In all three CS clumps, an associated IRAS point source dominates the 12- and 25-μm emission; however, new objects identified through their submillimetre continuum emission, and distinct from the 12- and 25-μm IRAS point sources, are major contributors to the observed, extended 60- and 100-μm IRAS emission. These results suggest that the previously classified 'Class I' objects actually consist of multiple sources at different evolutionary stages.

We were able to closely model the object IRAS 12 S1 using a single spike in all IRAS wavebands, with good spatial separation from other sources. Using the combined HIRES, SCUBA and millimetre fluxes to plot an SED with several reliable flux points on both the Wien and Rayleigh–Jeans sides of the peak, we have calculated the dust temperature, bolometric luminosity and circumstellar mass of this source. The SED and physical parameters of this source, together with its likely status as the principal driving source of outflow NGC 2264 D, suggest that IRAS 12 S1 is a Class 0 object harbouring one or more intermediate-mass protostars.

While it is not possible to derive individual SEDs for all of the embedded objects due to the presence of extended emission and source confusion, we can at least place good upper limits on the individual flux contributions and thus compare the new IRAS 'point source' luminosities to luminosities that were previously derived using IRAS Point Source Catalogue fluxes. In the two cases where the IRAS point source is not coincident with a submillimetre source, such a comparison indicates the IRAS source to be of significantly lower bolometric luminosity than previously estimated.

Our new CO $J = 2 \rightarrow 1$ outflow maps of the three regions that we studied indicate complex outflow morphology suggestive of multiple driving sources. We find that the submillimetre source, 12 S1, contributes to driving the NGC 2264 D outflow; however, the previously assumed driving source for this flow, the source at the IRAS PSC position (RNO), cannot be associated with any high-velocity CO emission. There are hints of three separate outflows in the vicinity of IRAS 25: a giant Herbig–Haro flow, probably powered by the near-infrared source that lies at the IRAS PSC position, and two very compact CO outflows that may be associated with the submillimetre sources 25 S1 and 25 S2. In the IRAS 27 region, the strongest submillimetre source (27 S1), which is also coincident with the IRAS PSC position, apparently drives the redshifted gas associated

with the outflow NGC 2264 H. The multilobed appearance of the blueshifted gas, and the morphology of the low-velocity redshifted gas, suggest the presence of two other outflows in this region: a bipolar outflow associated with 27 S2, and blueshifted gas that may be associated with 27 S3.

Our results have implications for the method of using outflow momentum deposition rates and source bolometric luminosities in order to infer the fraction of the accretion flow that is ejected into the wind of protostars, and thus for using this method to distinguish between different proposed launching mechanisms. It is clear that in many cases outflow momentum deposition rates cannot be unequivocally correlated with source luminosities in many of the clustered regions for which luminosities were derived using *IRAS* fluxes.

Six of the submillimetre objects identified in this paper can be associated with faint objects identified from the recently released Two-Micron All Sky Survey Point Source Catalogue. A detailed analysis of the physical properties and evolutionary status of these sources will be presented in a subsequent paper.

## REFERENCES

Adams F. C., Lada C. J., Shu F. H., 1987, ApJ, 312, 788
Allen D. A., 1972, ApJ, 172, L55
André Ph., Ward-Thompson D., Barsony M., 1993, ApJ, 406, 122
André Ph., Ward-Thompson D., Barsony M., 2000, in Mannings V., Boss A. P., Russell S. S., eds, Protostars and Planets IV. Univ. Arizona Press, Tucson, p. 59
Archibald E. N. et al., 2002, MNRAS, 336, 1
Aumann H. H., Fowler J. W., Melnyk M., 1990, AJ, 99, 1674
Bally J., Lada C. J., 1983, ApJ, 265, 824
Barsony M., Ward-Thompson D., André P., O'Linger J., 1998, ApJ, 509, 733
Blitz L., 1978, PhD thesis, Columbia Univ.
Bontemps S., André P., Terebey S., Cabrit S., 1996, A&A, 311, 858
Cabrit S., Bertout C., 1992, A&A, 261, 274
Cao Y., Prince T. A., Terebey S., Beichman C. A., 1996, PASP, 108, 535
Cao Y., Prince T. A., Terebey S., Beichman C. A., 1997, ApJS, 111, 387
Casali M. M., Eiroa C., Duncan W. D., 1993, A&A, 275, 195
Castelaz M. W., Grasdalen G., 1988, ApJ, 335, 150
Cohen M., Harvey P. M., Schwartz R. D., 1985, ApJ, 296, 633
Feldbrugge P. T. M., van Genderen A. M., 1991, A&AS, 91, 209
Holland, W. S. et al., 1999, MNRAS, 303, 659
Hurt R. L., Barsony M., 1996, ApJ, 460, L45
Jenness T., Economou F., 2001, www.jach.hawaii.edu/JACpublic/stardocs/sun231.htx/sun231.html
Jenness T., Holland W. S., Chapin E., Lightfoot J. F., Duncan W. D., 2000, in Manset N., Veillet C., Crabtree D., eds, ASP Conf. Ser. Vol. 216, ADASS IX. Astron. Soc. Pac., San Francisco, p. 559
Lada C. J., 1985, ARA&A, 23, 267
Levine D. M., Surace J., 1993, in IPAC User's Gui de, 5th edn. IPAC, Pasadena
Lorenzetti D., Giannini T., Vitali F., Massi F., Nisini B., 2002, ApJ, 564, 839
Lynds B. T., 1962, ApJS, 7, 1
McKee C., 1999, in Kylafis N. D., Lada C. J., eds, The Origin of Stars and Planetary Systems. Kluwer, Dordrecht, p. 29
Margulis M., Lada C. J., Snell R. L., 1988, ApJ, 333, 316 (MLS88)
Margulis M., Lada C. J., Young E. T., 1989, ApJ, 345, 906 (MLY89)
Mendoza E. E., Rodriguez L. F., Chavarria-K. C., Neri L., 1990, MNRAS, 246, 518
Mitchell G. F., Johnstone D., Moriarty-Schieven G., Fich M., Tothill N. F. H., 2001, ApJ, 556, 215
Moneti A., Reipurth B., 1995, A&A, 301, 721
Myers P., 1999, in Kylafis N. D., Lada C. J., eds, The Origin of Stars and Planetary Systems. Kluwer, Dordrecht, p. 67
Ogura K., 1995, ApJ, 450, L23
O'Linger J., 1997, MSc thesis, Univ. California, Riverside
O'Linger J., Wolf-Chase G., Barsony M., Ward-Thompson D., 1999, ApJ, 515, 696
O'Linger J., Cole D. M., Ressler M. E., Wolf-Chase G., 2003, AJ, submitted
Oliver R. J., Masheder M. R. W., Thaddeus P., 1996, A&A, 315, 578 (OMT96)
Panagia N., 1991, in Kylafis N., Lada C. J., eds, The Physics of Star Formation and Early Stellar Evolution. Kluwer, Dordrecht, p. 565
Pérez M. R., Thé P. S., Westerlund B. E., 1987, PASP, 99, 1050
Piché F., Howard E. M., Pipher J. L., 1995, MNRAS, 275, 711
Richards P. J., Little L. T., Toriseva M., Heaton B. D., 1987, MNRAS, 228, 43
Richer J. S., Shepherd D. S., Cabrit S., Bachiller R., Churchwell E., 2000, in Mannings V., Boss A. P., Russell S. S., eds, Protostars and Planets IV. Univ. Arizona Press, Tucson, p. 867
Rodríguez L. F., Reipurth B., 1998, Rev. Mex. Astron. Astrofis., 34, 13
Sagar R., Joshi U. C., 1983, MNRAS, 205, 747
Sandell G., 1994, MNRAS, 271, 75
Sargent A. I., Van Duinen R. J., Nordh H. L., Fridlund C. V. M., Aalders J. W. G., Beintema D., 1984, A&A, 135, 377
Schreyer K., Helmich F. P., van Dishoeck E. F., Henning Th., 1997, A&A, 326, 347
Surace J. A., Mazzarella J., Soifer B. T., Wehrle A. E., 1993, AJ, 105, 864
Terebey S., Mazzarella J., eds, 1994, Science with High Spatial Resolution Far-Infrared Data, JPL 94-11. JPL, Pasadena, CA
Testi L., Palla F., Natta A., 1999, A&A, 342, 515
Walker M. F., 1956, ApJS, 2, 365
Walker C. K., Adams F. C., Lada C. J., 1990, ApJ, 349, 515
Walsh J. R., Ogura K., Reipurth B., 1992, MNRAS, 257, 110
Wang H., Yang J., Wang M., Yan J., 2002, A&A, 389, 1015
Ward-Thompson D., Zylka R., Mezger P. G., Sievers A. W., 2000, A&A, 355, 1122
Williams J. P., Garland C. A., 2002, ApJ, 568, 259
Wolf-Chase G. A., Walker C. K., 1995, ApJ, 447, 244 (WW95)
Wolf-Chase G. A., Walker C. K., Lada C. J., 1995, ApJ, 442, 197 (WWL95)
Wood D. O. S., Churchwell E., 1989, ApJ, 340, 265

This paper has been typeset from a TEX/LATEX file prepared by the author.